WAVENUMBER RECOVERY BY FWI FROM SLOWNESS-LIMITED, AND SOURCE-FREQUENCY-LIMITED ELASTIC SEISMIC DATA

SASMITA MOHAPATRA and GEORGE A. MCMECHAN

Center for Lithospheric Studies, The University of Texas at Dallas, 800 W. Campbell Road, Richardson, TX 75080-3021, U.S.A. sasmita@utdallas.edu

(Received July 28, 2021; accepted October 25, 2021)

ABSTRACT

Mohapatra, S. and McMechan, G.A., 2021. Wavenumber recovery by FWI from slowness-limited, and source-frequency-limited elastic seismic data. *Journal of Seismic Exploration*, 30: 577-600.

Any feature in an elastic model can be extracted by full wavefield inversion (FWI) only if its physical wavenumbers (**k**) are also present in the illuminating and recorded wavefields. The effective incident wavenumbers contain the combined information in the incident wavefront directions (in the slownesses **p**) and in the frequencies ω (in the source time function). The fundamental relationship is **k** = ω**p**. Thus, the wavenumber spectral aperture of surface data can be increased by increasing the effective slowness aperture (e.g., by increasing the offset, or adding data from borehole recorders) and/or by increasing the frequency bandwidth of the source wavelet. For a given **k**, ω and **p** are not unique; an infinite number of (ω, **p**) pairs can provide the same **k**, but only if both are present. Because the acquisition geometry and the source spectral bandwidth are both discrete and finite, the wavenumber spectra of the inverted parameters of any target model can never be fully recovered by FWI; FWI images are always a bandlimited version of the complete solution. A prerequisite for minimizing cycle skipping in FWI is that the temporal and spatial sampling of the data and the model must be unaliased, and therefore satisfy the half-wavelength condition as the frequency is progressively increased during the FWI iterations. The phase of the data provides stronger constraints than the amplitude; thus velocities are better fitted than densities. Image correlation, and calculation of the correlation coefficient (R^2) of model images quantify the behavior of decreasing model misfits as iterations proceed. Synthetic elastic examples for models containing finite bandwidths illustrate how the ability to recover wavenumbers is limited by the wavenumber information that is contained in the illuminating wavefield, and by the sampling of the data in both time and space.

KEY WORDS: 2D, FWI, elastic, slowness, frequency, wavenumber.

0963-0651/21/$5.00

INTRODUCTION

This paper numerically quantifies the relationship between wavenumbers in an illuminating wavefield and the wavenumbers that are reconstructable in a target by migration or inversion. The larger objective is to optimize the source and receiver distributions for inversion of any specific target geometry, but this is beyond the scope of the present study.

Berkhout (1980), Hu and McMechan (1986) and Biondi and Almonon (2014) show how image resolution and completeness vary directly with recording aperture. Long-offset, wide-aperture (or azimuth) acquisitions present deployment and financial challenges. The quality and resolution of seismic images are limited by the temporal bandwidth and the radiation pattern of the source wavelet, the wave propagation attenuation, the acquisition geometry, and the response function of the recording instrumentation. Schuster and Hu (2000), Gibson and Tzimeas (2002) and Yu and Schuster (2003) perform resolution analysis using simplified model geometries, and ray-based, high-frequency, asymptotic methods. Seismic illumination analysis shares much in common with resolution analysis (Muerdter and Ratcliff, 2001a,b; Muerdter et al., 2001; Berkhout et al., 2001; and Volker et al., 2001). However, traditional illumination analysis focuses mostly on how the model space is covered by seismic energy without detailed consideration of image distortion caused by incomplete illumination.

McMechan and Hu (1986) show an example using data for a salt flank model that illustrates the effects of limited aperture recording, and then how a surprisingly good image can be obtained even from a single common source gather, by increasing the effective recording aperture by including left, right and surface recording in vertical seismic profiles (VSPs) and surface survey data. The partial images each give a different view of the structure that depends largely on the orientations of the structural elements relative to the recording aperture. The effects of the source frequency spectrum were not explicitly considered, and the feature resolution in the images was not evaluated.

The issues of reconstructing wavenumbers have previously been partially investigated in the context of diffraction tomography, in the form of analytic solutions (e.g., Slaney and Kak, 1983). These examples are limited to simple structures because the solutions are analytical rather than numerical. Diffraction tomography and inversion work best when sources and receivers surround the region of interest, as in medical imaging applications. Devaney (1984), Devaney and Beylkin (1984), Esmersoy et al. (1985), Esmersoy and Levy (1986), and Wu and Toksöz (1987) have shown that, in the seismic inverse problem, the velocity image will be only partially reconstructed with sources and geophones on the Earth's surface. Mora (1987, 1989) shows that only the high vertical wavenumbers are resolved by reflections; the inversion results look like migrations and do not resolve, but rather require as input, a priori smooth (low-wavenumber) initial velocity model.

Full waveform inversion (FWI) can construct a high-resolution subsurface image, provided that data with a broad frequency band, and wide-angle (in 2D) and azimuth (in 3D) apertures are available. FWI is pioneered by Lailly (1983), Tarantola (1984), and Fichtner (2010), among many others. The wave-propagation velocity model can be divided into two overlapping parts. The long-wavelength background model typically contains a smooth version of the complete model; thus is it assumed to be correct up to some wavenumber, and the overlapping portion is not required to be updated, but no change is predicted if it is included in the updates. The second part contains intermediate and short-wavelengths of the model that correspond to those in the recorded seismic wavefield.

Seismic imaging presents several limitations. Mora (1989) and Pratt et al. (1996) show that the long wavelengths of the model can be retrieved using long-offset and transmission data. The data must be unaliased in time, space, frequency and wavenumber and thereby satisfy Mora's (1987, 1989) half-wavelength criterion for avoiding cycle skipping. If the data lack low frequencies, then having the low wavenumber components in the starting model is necessary.

Alkhalifa (2016) uses linearized relations between accurately known model wavenumbers, and extracted wavenumbers obtained either from image-based methods such as RWI (reflected waveform inversion) or from classic FWI examples using data from the Marmousi model, and SEG2014 blind test data (the latter was built by Chevron and distributed in a workshop at the SEG annual meeting in 2014). Alkhalifa et al. (2018) analysed the potential sources of information for recovery of middle model wave-numbers, including regularization, objective function enhancements, and multiscattered energy. The data information includes large offsets and multiscattered energy, in which the energy through wavepath and scattering updates can admit more of the middle-wavenumber information that come from the data. Xu et al. (2020) have used three stage E-FWI (elastic full waveform inversion, ARTI (reflection traveltime inversion using acoustic wave propagator), and E-RWI (elastic reflection wave inversion approaches to recover low-, intermediate- and high-wavenumber components of P- and S-wave velocity models using multi-component reflection recordings.

Multi-parameter elastic FWI (EFWI) is more suitable for wide-aperture, multi-component seismic data than single-parameter scalar-wave (or acoustic) velocity FWI. The acoustic solution is not able to fit P-S mode conversions as they are not part of the acoustic parameterization. As more parameters are considered in elastic inversion, it is increasingly useful for geologic interpretation of rock properties (e.g., identification of lithologies), and for reservoir fluid characterization and monitoring. Density is the most difficult parameter to be inverted as it has no impact on the phase of the seismic field to be inverted (Forgues and Lambaré, 1997), and it is typically recovered from very low frequencies (below 1 Hz) along with other parameters (V_P and V_S) in elastic inversion. Choi et al. (2008), using synthetic data from the elastic Marmousi-2 model, show a successful reconstruction of density using an unrealistically low frequency (0.125 Hz).

Forgues and Lambaré (1997), Virieux and Operto (2009) and Warner et al. (2013) state that it is not easy to recover density in FWI because it is difficult to separate the effects of velocity and density as they are coupled in the impedance in reflection data. Jeong et al. (2012) estimate velocity and density from elastic FWI in the frequency domain. The product of velocity and density (the seismic impedance) determines the amplitudes of reflected seismic waves (Virieux and Operto, 2009; Xu and McMechan, 2014).

To investigate the potential application to realistic earth structures, we utilize these spectral interactions in numerical form, and thus produce quantitative examples and evaluations. The FWI studies listed above tend to focus on either the contribution, to model wavenumbers in the illumination, associated with the propagation direction of the incident wavefields as parameterized in the slowness vector **p**, or in the recording aperture.

NUMERICAL SOLUTIONS

To quantify the effects of **p** and ω, in the incident wavefields, on the quality and completeness of the FWI solution, a group of numerical examples is calculated for a two-dimensional elastic model with a circular anomaly (Fig. 1), and for the Marmousi-2 model. Two acquisition configurations for each of the circular anomaly and for the Marmousi-2 model are used as a function of source frequency bandwidth.

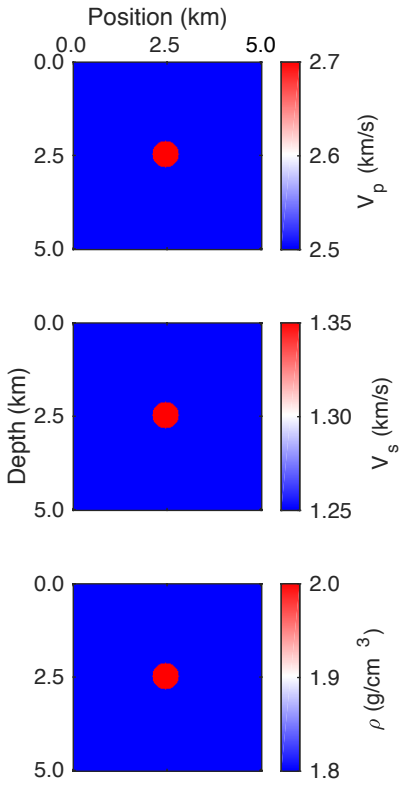

Fig. 1. Test elastic model with a circular anomaly. This contains a wide range of wavenumbers.

Frequency-domain full-waveform inversion (e.g., Pratt et al., 1996; Xu and McMechan, 2014) is well established for imaging 2D media in the frequency domain. The present paper follows this methodology to do simultaneous FWI for three elastic parameters: P-velocity (V_P), S-velocity (V_S) and density (ρ) using time-domain full-wavefield modeling of common-source gathers, which are then inverted in the frequency domain. Refer to Xu and McMechan (2014) for the theoretical aspects of this FWI.

A hybrid absorbing boundary condition which combines a damping zone (Shin, 1995), with a second-order elastic one-way wave-equation boundary equation (Higdon, 1991) is placed around the four edges of the model (Xu and McMechan, 2014, Brossier et al., 2009; Shin, 1995) to reduce unwanted model edge reflections, and free-surface effects (i.e., surface waves and body-wave reflections from the free surface) that increase nonlinearity in inversion. In all the examples below, this hybrid absorbing boundary is applied at all four grid edges.

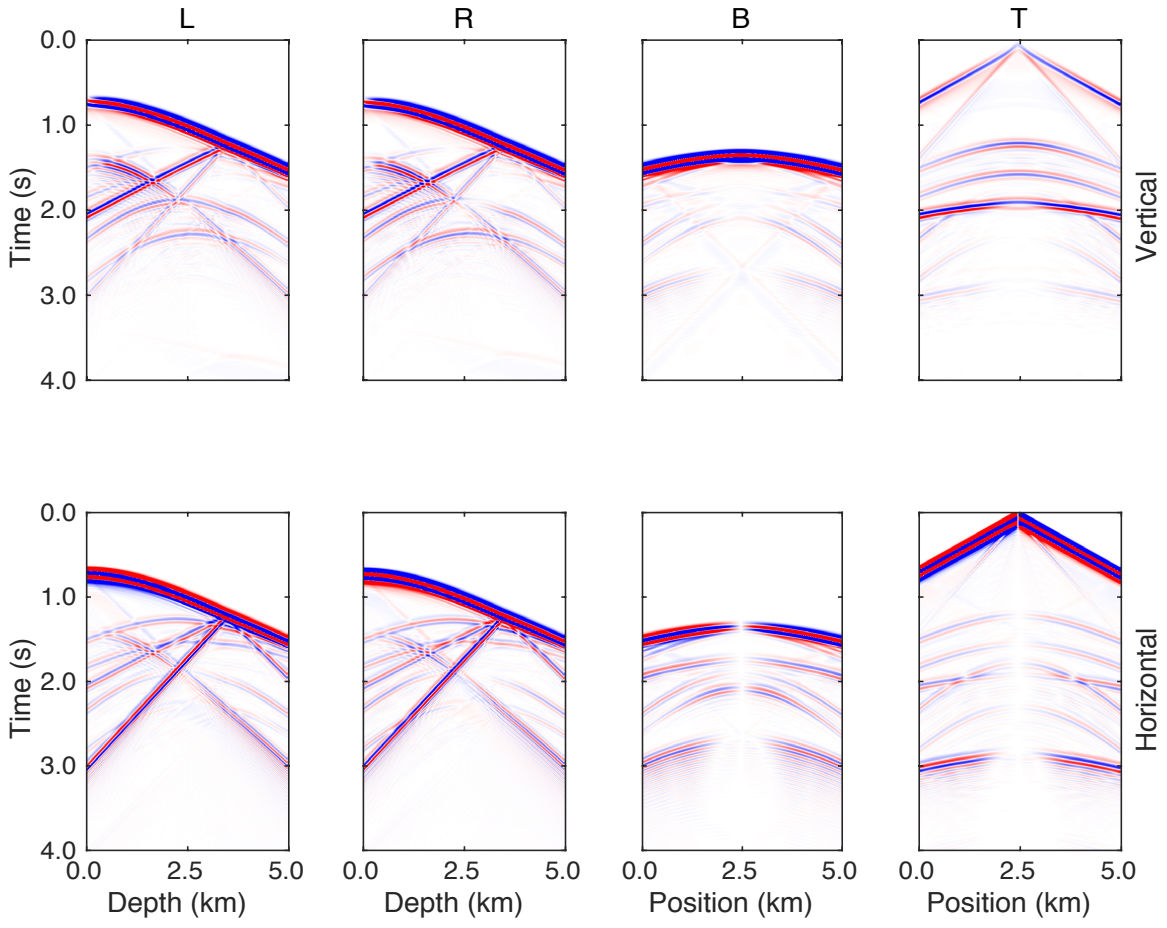

Fig. 2. The upper half contains the synthetic vertical-component and the lower half contains the synthetic horizontal-component elastic particle-displacement wavefields computed by finite difference modeling. Each row is composed of four representative subprofiles, all generated by the same source. Together, the four subprofiles form a single common-source gather recorded on geophones that surround the target above (Fig.1) on its top, bottom, right and left (T, B, R, and L) edges.

To illustrate the effects of recording aperture on the completeness of the inverted images we first consider the responses of a circular anomaly illuminated by a single source at a depth of 0.0 km recorded by two-component recorders deployed along each of the top, and the bottom surface, and the left and right edges of the model (Figs. 2 and 3). In the second example we use the same circular anomaly but simulate a complete survey aperture constructed by evenly distributing sources and 2-component receivers along each of the four grid edges. In the third example we consider the Marmousi-2 model (Martin et al., 2002) with two different survey apertures. In the first aperture, all the sources and recorders are deployed only along the upper surface of the Marmousi-2 model. The second aperture includes an additional 33 sources and 66 recorders along each of the upper portions of the left and the right edges of the model.

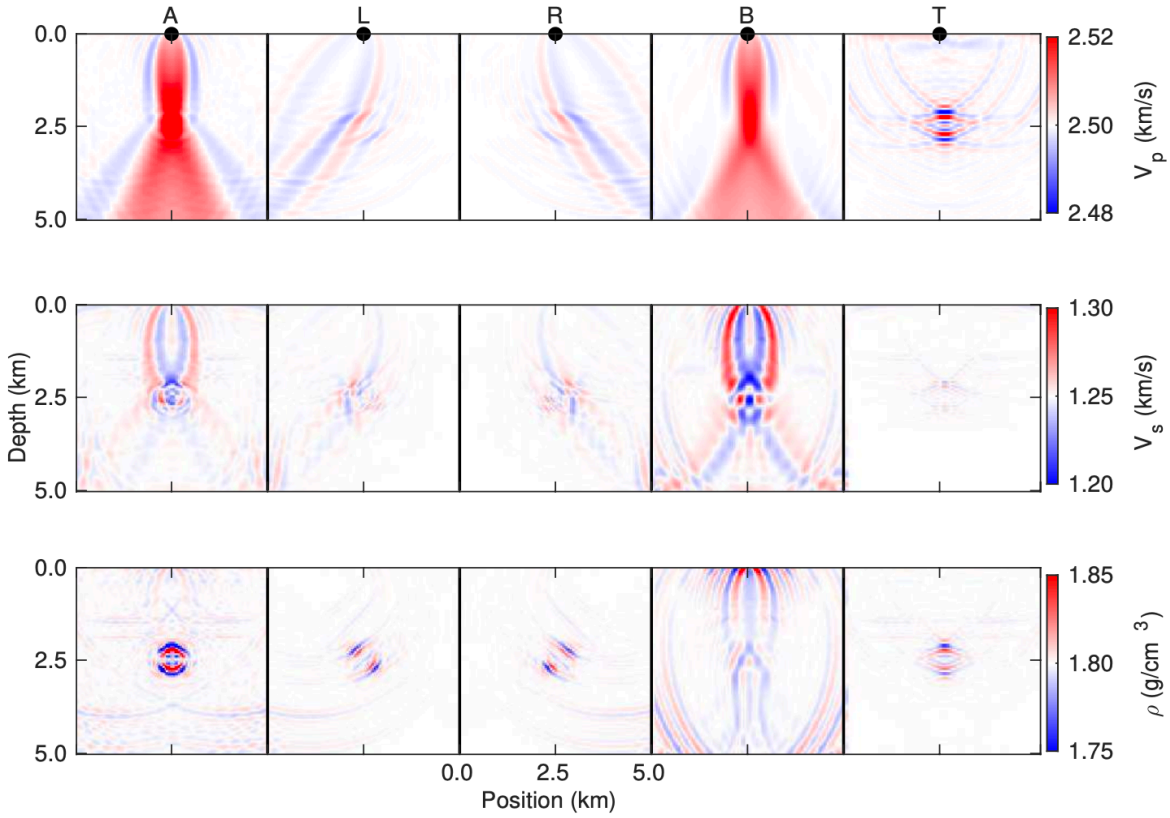

Fig. 3. Propagation velocity and density images obtained by inverting data from a single source (black dot), in five different recording apertures. Compare with the target structure in Fig. 1. (A) is the image obtained for the data from recorders placed along all four edges; (L) is from the left edge only, (R) is from the right edge only, (B) is from the bottom edge only, (S) is from the top surface only. The source (the black dot) is at depth of 0.0 km, and horizontal position 2.5 km.

The wavenumbers in both the model and in the illuminating wavefield contain combinations of the slowness (**p**), and frequency (ω). Below we exploit this characterization of wavenumber by varying both **p** (by changing the recording aperture) and ω (by progressively increasing ω) in frequency

domain FWI. The latter also reduces the likelihood of cycle skipping between frequencies. To quantify the differences between the known and predicted models and their corresponding 2D or 3D Fourier spectra, are displayed in image correlation (IC) plots (Liner, 2012), for which correlation coefficients (R^2) are calculated.

Example 1: Effects of recording aperture on recovery of a circular anomaly with data from a single source

To illustrate 2D FWI we begin with simple velocity models containing a circular inclusion in a homogeneous background (Fig. 1). The model is discretized on a 200×200 grid with a grid interval of 25 m. Thus the total number of unknowns for V_P, V_S and ρ in the inversion is 200×200×3. The circular anomaly has V_P of 2700 m/s, V_S 1350 m/s, and ρ of 2000 kg/m^3 in a background with V_P of 2500 m/s, V_S of 1250 m/s, and ρ of 1800 kg/m^3.

The starting model for the inversion is the homogeneous background. Thirty equally spaced frequencies from 1.46 to 10.57 Hz with a constant increment of 0.326 Hz are used. The source time signature is a Ricker wavelet with a dominant frequency of 6 Hz. The time sample increment is 0.0015 s and the total recording time duration is 4 s (Fig. 2).

To illustrate the effects of the recording aperture on the completeness of the inverted images, 200 two-component recorders are deployed with 25 m spacing along each of the top (T), and bottom (B) surfaces, and the left (L) and right (R) edges, of the model. Subsets of the synthetic data (Fig. 2) were inverted using the elastic FWI (EFWI) algorithm of Xu and McMechan (2014). For comparison, a fifth configuration (A), contains the complete aperture composed of all four of T, B, L and R. Fig. 3 contains inverted V_P, V_S, and ρ partial images obtained using each of the limited recording apertures, and using the composite aperture A, to record data from a single source deployed on the upper surface, at 2.5 km distance and 0.0 km depth.

The inversion involves iterating through a number of concurrent updates of V_P, V_S, and ρ across all sources using 30 frequencies with an equal interval of 0.326 Hz, during which the least-squares objective function (the residual between the observed and predicted frequency wavefields) is progressively minimized. Each element of the gradient vectors is the derivative of the objective function with respect to the corresponding current model parameters; a separate gradient is calculated for each elastic parameter at each iteration. Updates to the model parameters use different step lengths for each parameter, obtained by parabolic fitting to minimize the data misfit.

One iteration involves updating the P- and S-velocities and density once, with one set of gradients and steplengths, using data of 30 frequencies of 1.46 - 10.56 Hz for all sources. Convergence is defined, for the frequency band of 1.46 - 10.56 Hz, as the condition where the misfit no longer decreases, and the predicted updates are ~zero; a few, to a few tens of,

iterations are usually required for convergence of each frequency and each acquisition configuration. When convergence is achieved the corresponding model is used as the starting model for the next iteration. If the frequency steps are sufficiently small to avoid cycle skipping, the misfits of the objective function should decrease, and the resolution of the model should increase, with increasing iterations, with increasing bandwidth.

The inverted models for each of the recorder configurations for a single source at convergence for each frequency are shown in Fig. 3. The limited wavenumber apertures produced by the single source and the single edge (L, R, B, or T) receiver arrays give dip-limited views of the circular target corresponding to their respective scattering angle apertures. The V_P and V_S partial images contain different orientations because their polarizations are different. The B configuration produces strong transmission artifacts, which also appear in the A configuration (the complete recording aperture) because of the predominance of direct, near vertical propagation with some diffraction, as opposed to higher angle scattering for the given single source. These transmission artifacts can be treated as data in tomographic velocity estimation. At all the frequencies used and using the lowest V_P and V_S in the model, the half wavelength ($\lambda/2$) condition is satisfied, so cycle skipping is avoided.

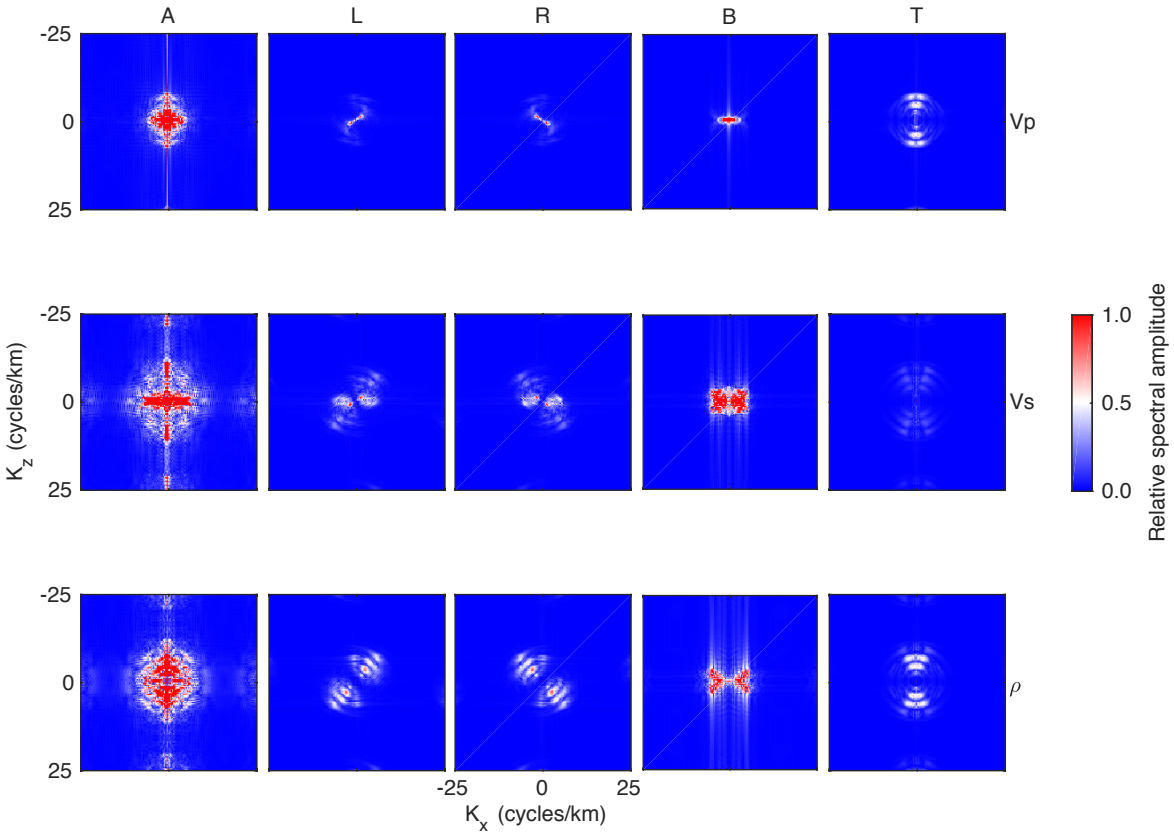

Fig. 4. Recorder-location-dependent spectral amplitudes for the inverted images for one source (at the black dot in Fig. 3). The ($\mathbf{k_x}$, $\mathbf{k_z}$) panel layouts correspond to the same relative positions as in the corresponding input (x, z) panels in Fig. 3.

The Fourier spectra panels in Fig. 4 are plotted in the same relative positions as their input V_P, V_S, and ρ images in Fig. 3. The value plotted at each point in each ($\mathbf{k_x}$, $\mathbf{k_z}$) spectrum is the relative magnitude of the complex Fourier component at that ($\mathbf{k_x}$, $\mathbf{k_z}$) location. In the single source responses in Figs. 3 and 4, each partial image and spectrum gives a different view of the structure that depends largely on the relative locations of the source, the structural elements, and the receiver aperture. The wavenumbers with the highest amplitudes correspond to the dominant direction of spectral scattering associated with the combination of the illumination direction from the single source, and the subsequent scattering aperture that is recorded in each of the two-component receiver apertures.

Example 2: Effects of multi-source arrays on FWI of a circular anomaly

In this example, inversion is performed for the same circular model as in Example 1. To get a more complete reconstructed image than in Example 1, we use a complete (but discrete) survey aperture constructed by evenly distributing, 200 sources and 200 2-component receivers (with 25 m increments) along each of the four grid edges, for a total of 800 recordings of each of the 800 sources. Both the source and receiver spacings in space, and the source wavelet sampling in time, are required to be unaliased, and thereby, to satisfy the half-wavelength condition (Mora, 1987) for both the P- and S-waves at the highest frequency in the data, and the lowest S-wave velocity in the model. The wavenumber vector **k** depends on the propagation direction, which is the slowness direction **p**(= 1/**v**), and on the frequency (ω); $\mathbf{k} = \omega\mathbf{p}$.

Thirty equally spaced frequencies from 1.46 to 10.56 Hz are used. The updated V_P, V_S and ρ models obtained at each iteration are the starting models for the next iteration. The left column in Fig. 5 contains the inverted space-domain V_P, V_S and ρ models, and the right column contains the % misfit between the true and inverted models; the maximum misfits occur along the edge of the anomaly, and correspond to the missing higher wavenumbers. Velocities are overestimated inside the anomaly, and density is underestimated. This is consistent with the fact that scattered data amplitudes (which are fitted in the objective function) depend on the P- and S-impedance contrasts, rather than the individual velocities and densities. The average misfits for V_P, V_S and ρ at convergence are approximately 0.2041 km/s (+7.5%), 0.1039 km/s (+7.69%) and -0.2737 g/cm^3 (-13.68%), respectively.

In the spectral representations of the true and inverted models (Fig. 6), and in the spectral misfits in the left column of Fig. 7, the differences are on the order of a few %, with the inverted values biased toward larger V_P and V_S and smaller ρ spectral values. In the left column of Fig. 7, the V_P and V_S spectral differences are mostly positive where the ρ spectral difference is mainly negative so they compensate for each other in their respective impedances. In the image correlation (IC) plots (Liner, 2012) in the right

column of Fig. 7, the original and inverted V_P and V_S spectra have high correlation coefficients, and the ρ coefficient is lower; this suggests that the velocities dominate the solution, and the misfits accumulate in the density, or equivalently, that the phase of the data provides stronger constraints than the amplitude (because density affects the amplitude, but not the phase).

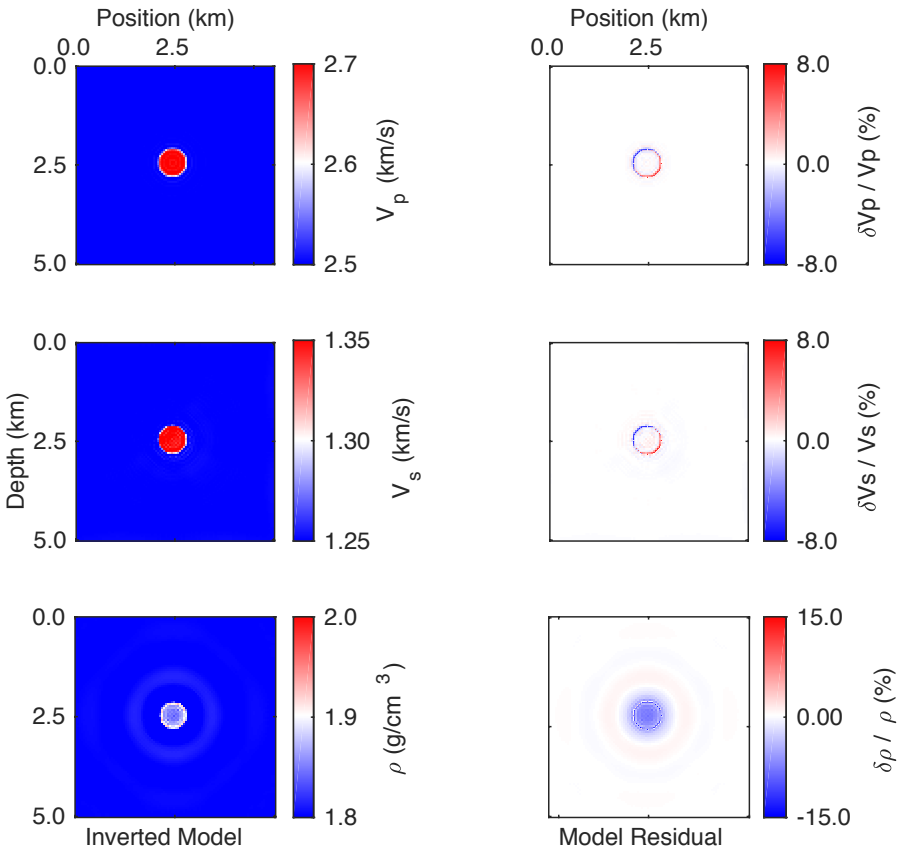

Fig. 5. The left column contains the inverted V_P, V_S and ρ models obtained using source and receiver apertures that completely surround the target; compare with the correct solution in Fig. 1. The right column contains the model residual between the correct and inverted models expressed as a % of the correct model.

The wavenumbers (**k**) in the inverted model are limited by the frequency (ω) bandwidth (since ω = **k**/**p**) of the source time function. Thus, the spectral bandwidths of the inverted V_P, V_S and ρ are always smaller than those of the corresponding true model; compare the left and right columns in Fig. 6. Also for any given frequency, V_S is always lower than V_P as (k_S/k_P = V_P/V_S), so the S-wavenumber bandwidth corresponding to the same frequency is always larger (farther from the origin of the plot) than that of the P-wavenumber (Fig. 6). Compare the spectral radii in the first and second rows of Fig. 6. To preserve the impedance values, the recovered spectral radius of ρ is smaller than those of V_P and V_S.

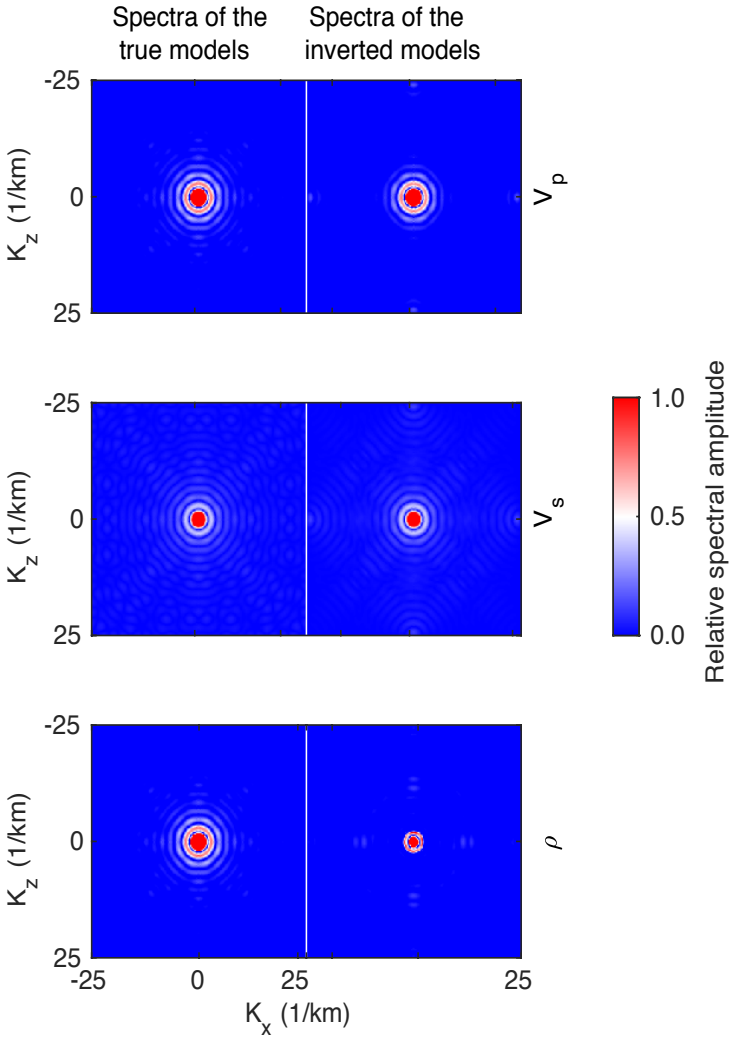

Fig. 6. The left column contains the Fourier spectral magnitudes of the true V_P, V_S and ρ circular anomaly models in Fig. 1; the right column contains the Fourier spectral magnitudes of the inverted models shown in the left column of Fig. 5. The inversion is done for unaliased sources and recorders surrounding the circular target.

In the impedance (Fig. 8), the inverted ρ with (R^2 = 0.33568) and the inverted velocities with (R^2s of 0.90142 for V_P and 0.89126 for V_S) interact. Propagation times are determined mainly by the velocities (although ρ is embedded in the denominator of the velocity expressions). Both ρ and the velocities contribute to the reflection amplitudes through their products $V_P\rho$ and $V_S\rho$, which are the impedances. Thus we calculate the impedances I_P and I_S (Fig. 8) from their velocity × density products. It is also possible to directly invert for impedances (I_P and I_S) as two separate parameters. The third column in Fig. 8 contains the fractional misfits of I_P and I_S, expressed as a percent of the true values. The R^2 values for the residual impedance (0.78697 for I_P and 0.77688 for I_S, corresponding to the first and second columns of Fig. 8), are intermediate between those of the density and velocities, as expected.

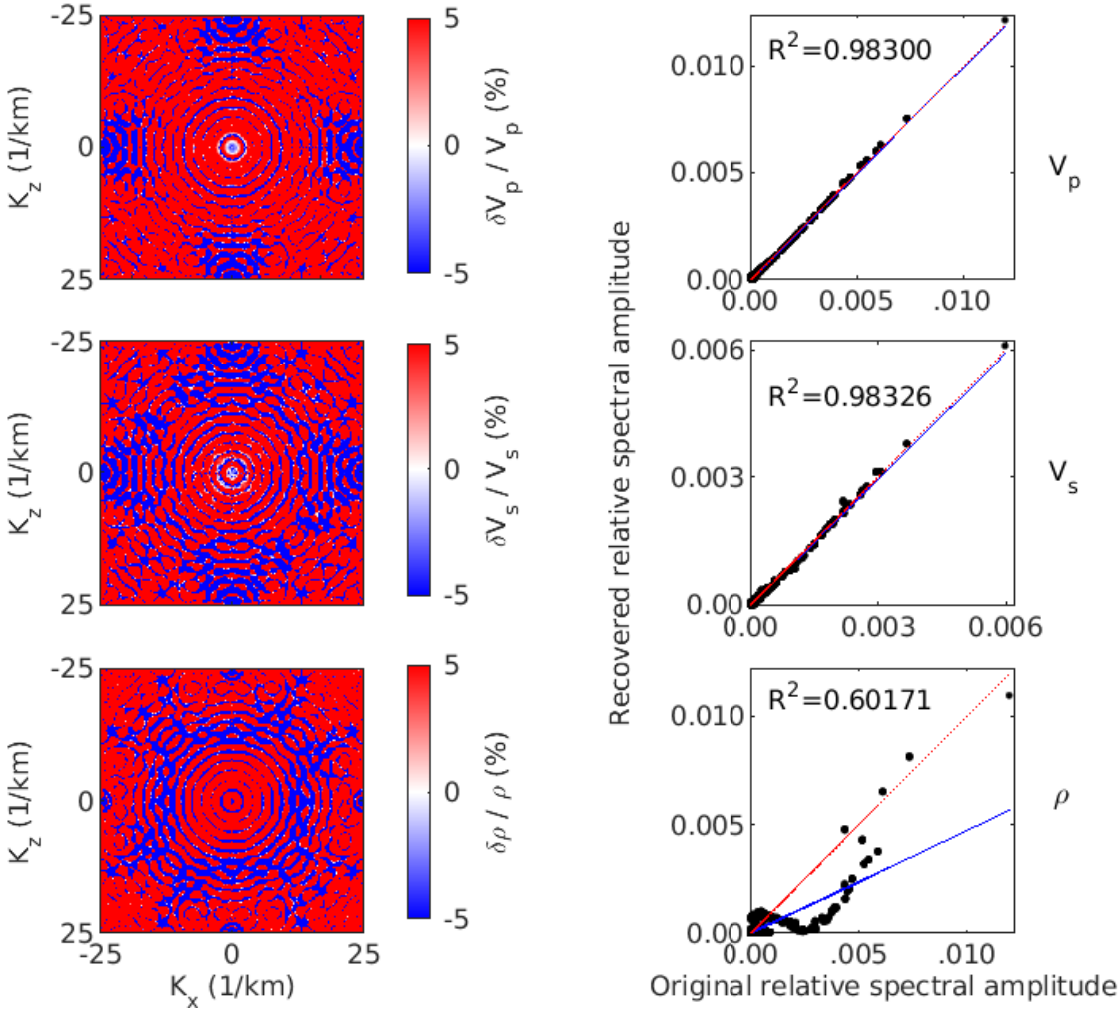

Fig. 7. The left column contains the residual between the actual and inverted spectral magnitudes (in Fig. 6) expressed as % of the correct spectra. The right column contains the image correlation between the true and the inverted spectra in Fig. 6; in the right column, the red lines are the ideal relations where the misfits are zero and the blue lines are the least squares regressions to the data points.

Example 3: Iterative elastic inversion of synthetic data from the Marmousi-2 model

To illustrate the concepts described above in a more realistic context, in this section, we apply the procedure to synthetic data for the elastic Marmousi-2 model (Martin et al., 2006) in the first column of Fig. 9. The elastic EFWI software used here was previously applied to the Marmousi-2 model by Xu and McMechan (2014); here we design examples to illustrate the consequences, on the elastic inversion results, of two different survey apertures, and two different frequency bands.

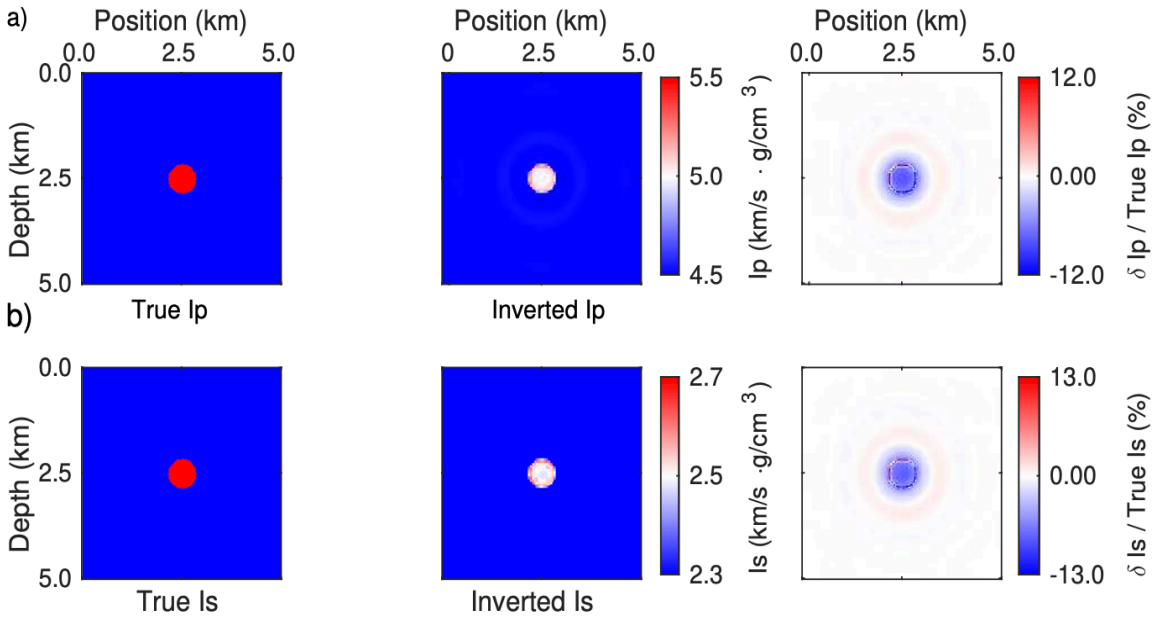

Fig. 8. The true and inverted (a) I_P and (b) I_S impedances from the products of the velocities and densities (in Figs. 1 and 5, respectively) at convergence. The third column contains the fractional errors of the impedance misfits. The largest residual misfits for I_P are ~11.3%; the largest misfits for I_S are ~12.6%.

Effects of survey aperture and source bandwidth in the position-depth (x-z) domain

The first survey aperture considered contains 111 explosive surface sources (Ss) spaced every 0.04 km, and 231 receivers (Rs) spaced every 0.02 km, along the surface of the model. The second survey aperture contains the first, but also includes 33 explosive sources every 0.04 km spacing along the upper 1.32 km of each of the left and the right vertical edges of the model. Each source is recorded by 231 receivers along the surface and 66 along the upper 1.32 km of each of the left and right edges, all at 0.02 km spacing. The presence of reflectors in the model partially compensates for not having sources and geophones along the bottom of the model, by generating up going reflected waves that are included in the inversions.

The starting models for the EFWI for the V_P, V_S and ρ are the same as those in Fig. 4 of Xu and McMechan (2014) and are generated by smoothing the true models using a 2D Gaussian filter with a correlation length of 1.6 km. Each source is excited in turn with a Ricker time wavelet with a dominant frequency of 6 Hz, and a maximum frequency 12.218 Hz. The time sample increment is 0.0015 s, and the frequency sample increment is 0.326 Hz. The total source frequency bandwidth is [3.09-12.218] Hz. For comparison, the frequency bandwidth used in FWI by Brossier et al. (2009), is [1.7-7.0] Hz, and by Pageot et al. (2013) is [0.05-0.4] Hz.

Columns two through five in Fig. 9 (a, b and c) contain the final results of the inversions at convergence; V_P and V_S have smaller misfits when the Ss and Rs are located along the surface and the two edges compared to the results obtained when the Ss and Rs are placed only along the surface. Also, as seen in Fig. 9, the images obtained with the full 3.09 to 12.218 Hz bandwidth data are much closer to the correct solutions (especially for density) than those obtained for the partial bandwidth (3.09 to 7.654 Hz) solutions because the wavenumber range in the former is larger. To compare the reconstructed models with the true model, the corresponding IC plots are shown in Figs. 10a and 10b. The R^2 values are consistently slightly higher when the Ss and Rs along the surface and the two vertical grid edges are used compared to when data from any only the surface Ss and Rs are used.

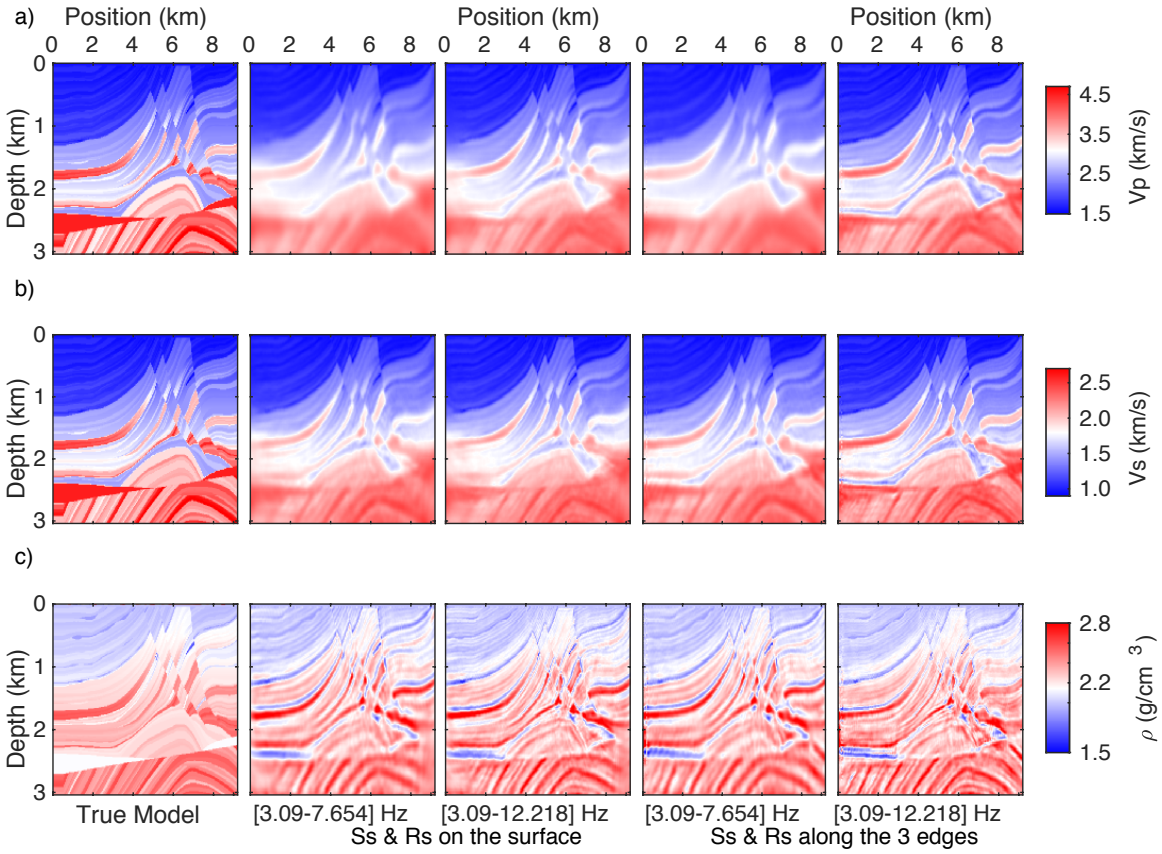

Fig. 9. The left column contains the true Marmousi-2 model. The second and third columns contain the inverted images of data with sources (Ss) and recorders (Rs) only on the surface. The fourth and fifth columns contain the inverted images of data with sources and recorders along the surface and the left and right edges. (a) are the V_P images, (b) are V_S and (c) are ρ, all obtained using the two-component synthetic common-source gathers.

The geometrical distributions of data points in Fig. 10 show the point density distribution misfits in a 61x51 bin, between the distributions of the estimated V_P, V_S and ρ (in column 5 of Fig. 9), and the true model values (in column 1 of Fig. 9). The shift in position of each data point off the red line

corresponds to the misfit of that model parameter. The gray scale gives the data density, the number of data points with the sampling box centered at that location. The horizontal gaps in data density between vertical lines of constant true model values in Fig. 10 correspond to velocities and densities that are not in the original (non-smooth) model parameters (in the left column of Fig. 9). The vertical extent of the data distributions along the constant original model value lines in Fig. 10 indicate the range of uncertainties in the corresponding inverted model parameter values.

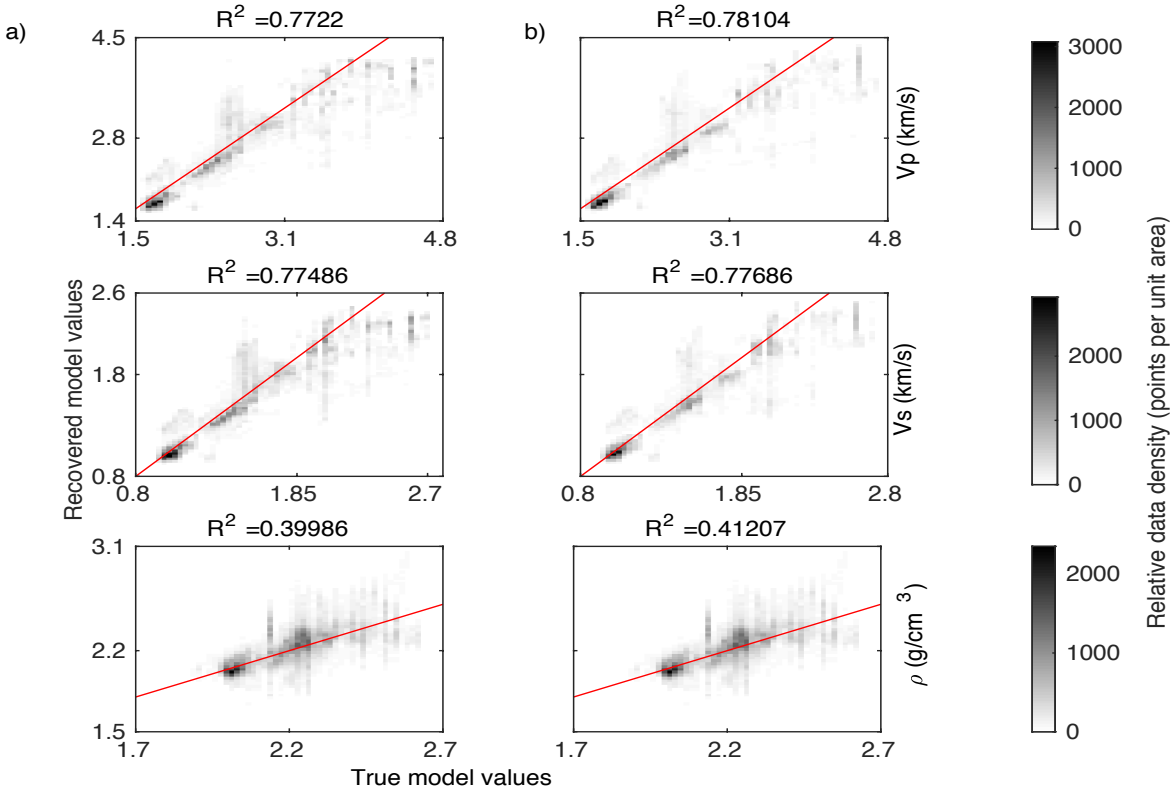

Fig. 10. The IC plots between the true and inverted model velocities and density for (a) Ss and Rs on the surface only and (b) Ss and Rs along the surface and the two edges, for the images shown in Fig. 9 for V_P, V_S and ρ for the frequencies from 3.09 to 12.218 Hz. In each panel, the red line is the theoretical location of perfectly recovered elastic parameters.

Effects of survey aperture and source bandwidth in the wavenumber $(k_x - k_z)$ *domain*

Fig. 11 contains Fourier spectral amplitudes of the true model and the full 3.09 - 12.218 Hz bandwidth solutions shown in Fig. 10 for both of the S/R configurations. When the recording aperture is limited to surface Ss and Rs, the spectra (Fig. 11b) have correspondingly smaller bandwidths, compared to the full spectra (Fig. 11a), especially in $\mathbf{k}_z$. Expanding the source and recorder apertures to include the two vertical edges increases the wavenumber bandwidth in the inversion (Fig. 11c) by improving the range of recovery of the dips in the features in the model compare (Figs. 9b and

9c), but is still not as complete as that of the true model (Fig. 11a). Also compare columns 2 and 3 with columns 4 and 5 in Fig. 9.

The wavenumber spectra of the true model parameters (Fig. 11a) are complete up to the Nyquist sampling of the wavenumber in the models; these spectra are defined independently of any subsequent partial illumination produced by incomplete ω or **p** data. Thus, the reduction in the bandwidth of **k** in FWI can be thought of as a filtering of the complete spectra by ω- and/or **p**-limited operators associated with the limited ω-bandwidth of the source, and/or the limited **p**-aperture of the data acquisition. The recovered wavenumbers (**k**) are limited by the source frequency (ω) bandwidth, and, the slowness (**p**) in the data aperture used in the inversion (as **k** = ω **p**).

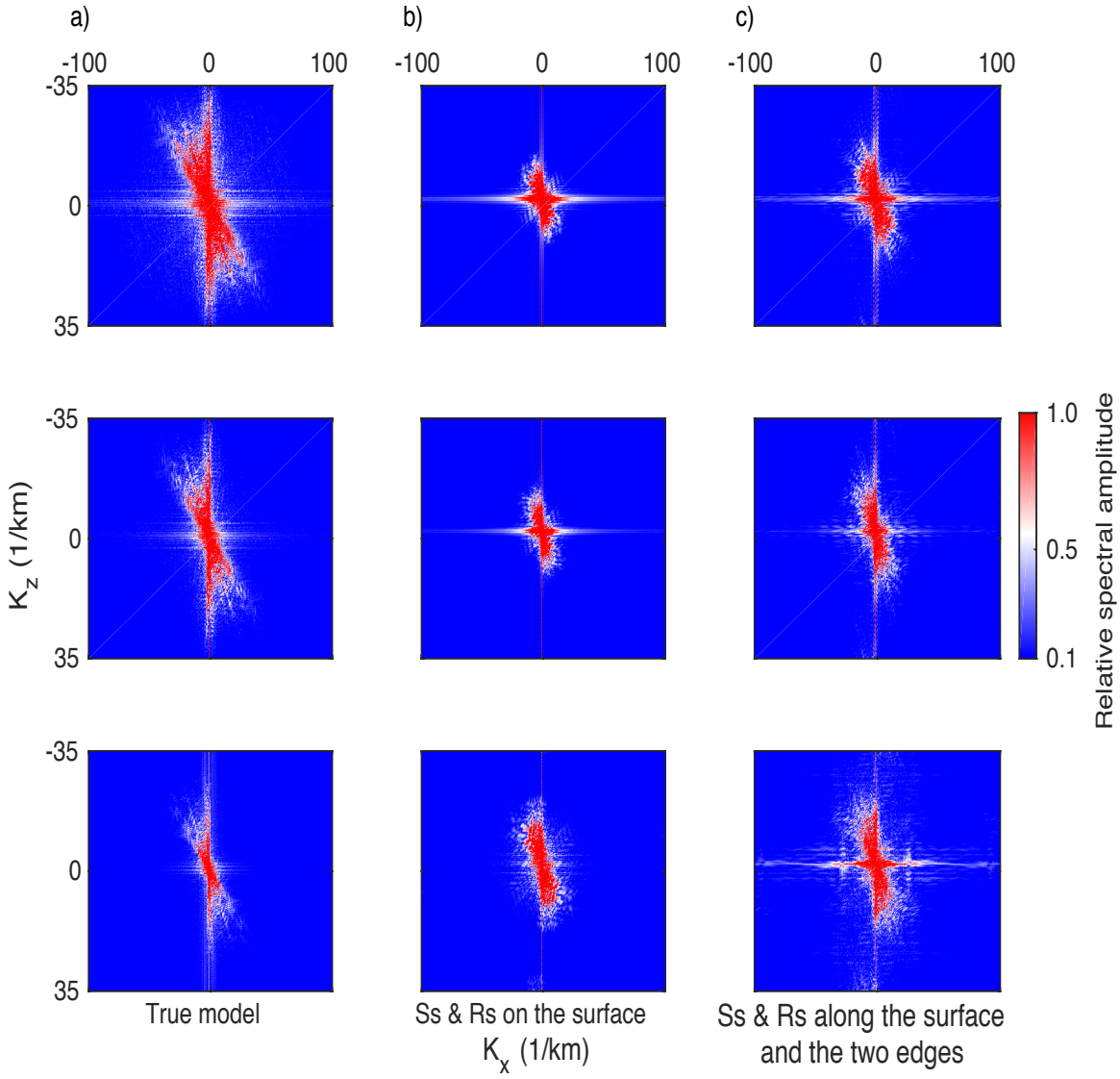

Fig. 11. Fourier spectral amplitudes as a function of wavenumbers of the images shown in Fig. 9 for V_P, V_S and ρ. Column (a) contains spectra of the true model, column (b) contains the spectra of the inverted model from the data for the Ss and Rs on surface, and column (c) contains spectra of the inverted model from the data for the Ss and Rs along the surface and the two edges of the Marmousi-2 model. The upper row is for V_P, the middle row is for V_S, and the bottom row is for ρ_P.

Spatial distribution of wavenumber recovery as functions of spatial aperture and frequency

Fig. 12 contains the residual misfits between the true and the inverted models for both S/R configurations using the full (3.09 - 12.218 Hz) frequency range (in the third and fifth columns of Fig. 9). The maximum misfits for V_P, V_S and ρ are approximately 1.7 km/s, 0.9 km/s and 1.24 g/cm^3, respectively; these misfits are concentrated along the reflectors, and are a consequence of the effective smoothing of the inverted models compared to the true models, caused by the missing wavenumbers.

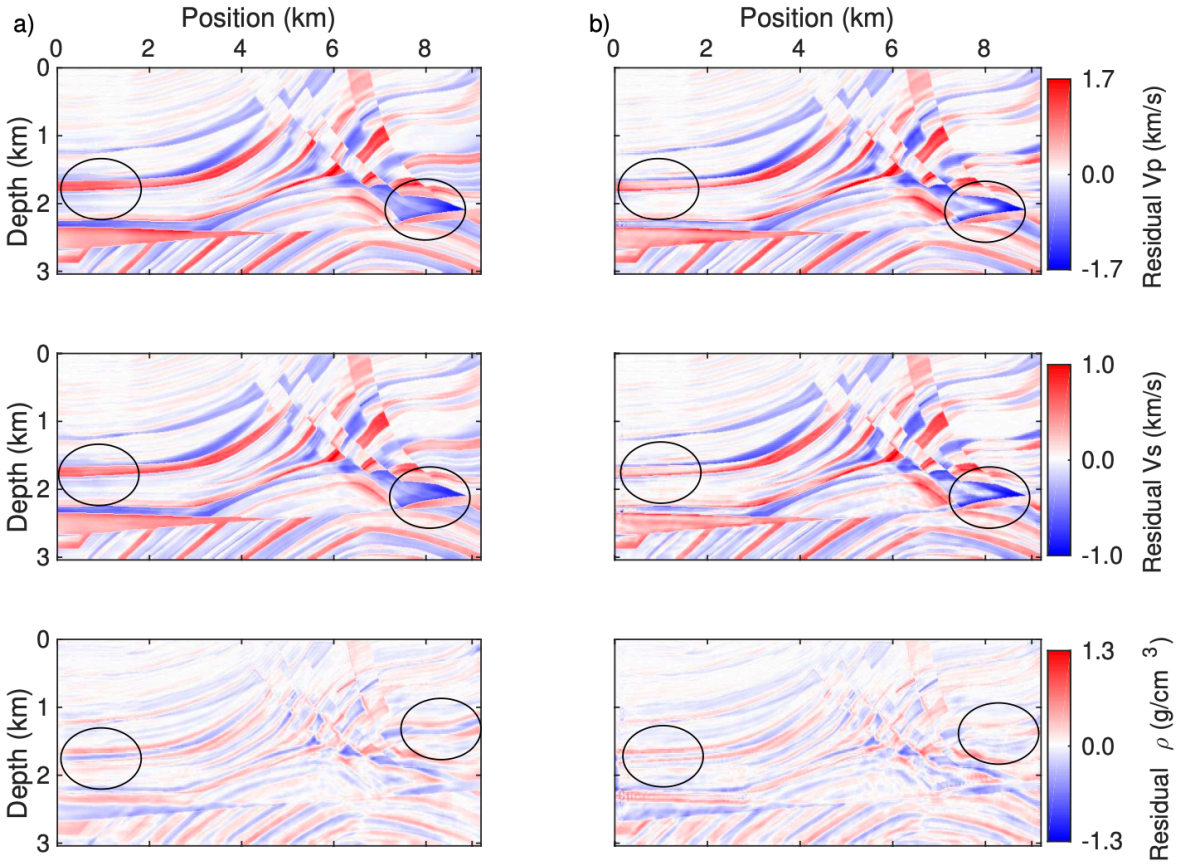

Fig. 12. The spatial distributions of V_P, V_S and ρ residuals which correspond to the parts of the model that are not recovered by inversion for (a) Ss and Rs on the surface only (the difference between columns 3 and 1 in Fig. 9) and for (b) Ss and Rs along the surface and the two edges (the difference between columns 5 and 1 in Fig. 9). Both (a) and (b) use the full frequency range.

As expected, the velocity and density residuals for the images in the left column in Fig. 12 are generally larger than those in the right column, because of the larger effective aperture in the latter. The differences between them are smaller where the reflectors are relatively flat, or near the center of the aperture, because the surface Ss and Rs contain most of the salient information in these areas. Dipping reflectors near the right edges are more accurately recovered when data from the two vertical lines of receivers are included (Fig. 12b) because this information is not recorded along the

surface (Fig. 12a). Compare in the ovals in Fig. 12. The residuals are smaller, especially for density near the two model edges, when data are recorded along those edges.

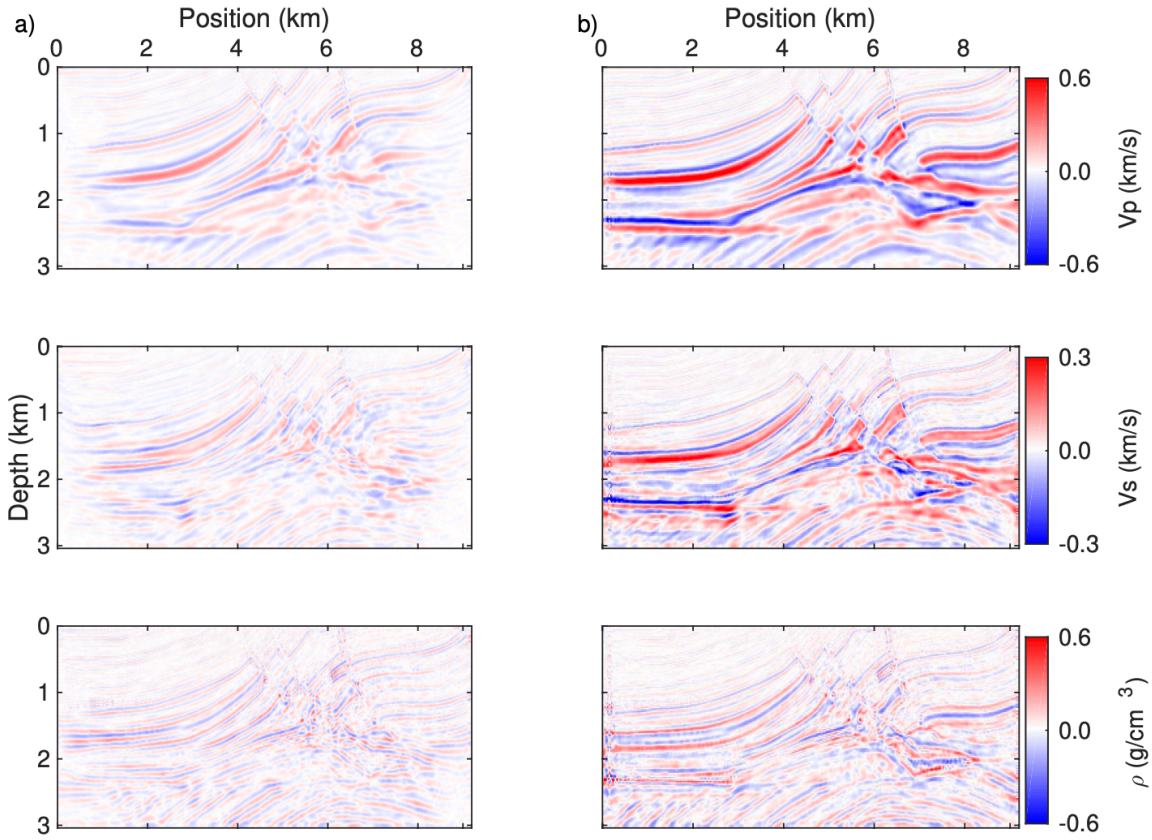

Fig. 13. The spatial distributions of the improvement in the inversion results obtained by increasing the frequency window from 3.09-7.654 Hz to 3.09-12.218 Hz for (a), using the Ss and Rs only on the surface (the difference between columns 2 and 3 in Fig. 9), and for (b), using the Ss and Rs also along the edges (the difference between columns 4 and 5 in Fig. 9). The image improvement values are larger in (b).

Fig. 13 contains the improvements obtained by increasing the maximum frequency when using the Ss and Rs (a) only along the surface, and (b) along the three edges. The maximum improvements in V_P, V_S and ρ are approximately 0.604 km/s, 0.29 km/s and 0.578 g/cm^3 respectively, and occur for the expanded (three-edge) aperture in Fig. 13(b). Fig. 14(a) contains the improvements obtained by increasing the acquisition aperture when using only the low frequency window. Fig. 14(b) contains the improvements obtained by increasing the acquisition aperture when using the full frequency window. The maximum improvements for V_P, V_S and ρ are approximately 1.2 km/s, 0.99 km/s and 0.396 g/cm^3, respectively, and occur for the full frequency window in Fig. 14(b). In this example, the impact in model fitting is much larger for increasing the acquisition aperture (Fig. 14) than for increasing the frequency bandwidth (Fig. 13); note the different ranges on the color bars.

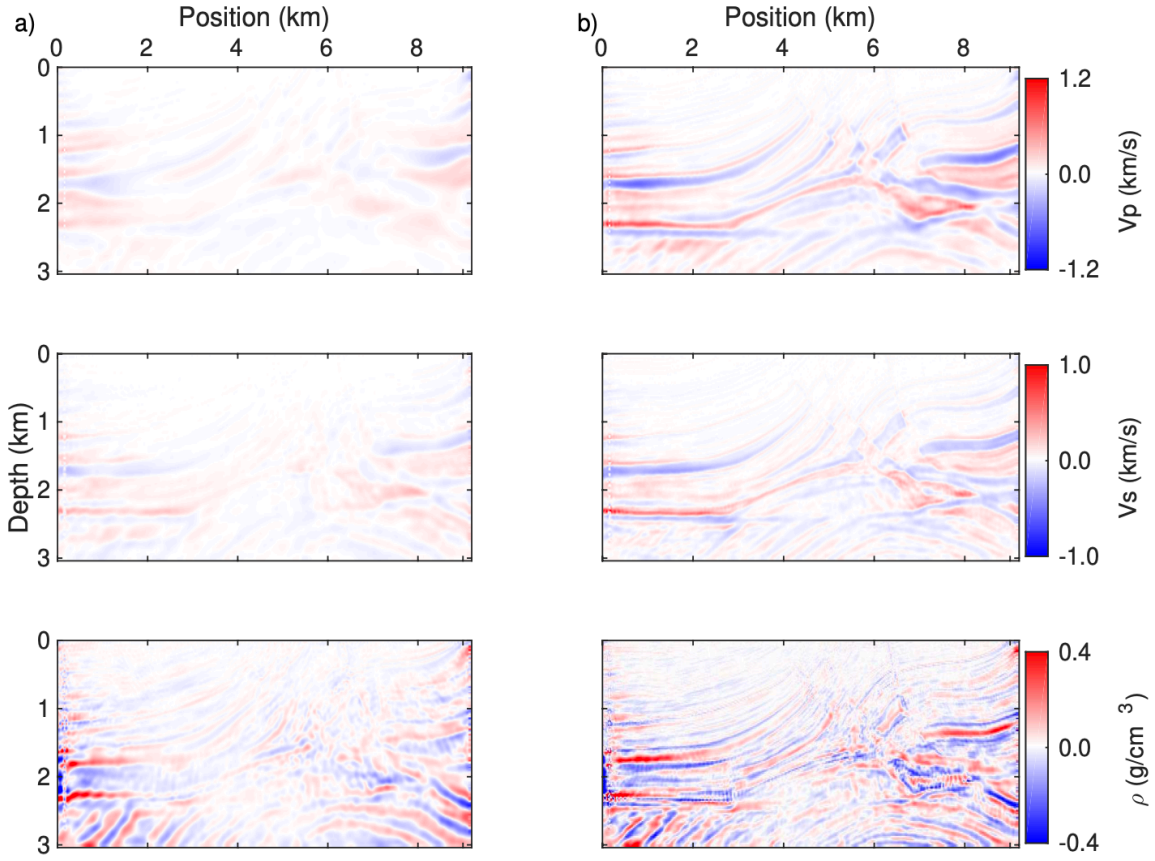

Fig. 14. The spatial distributions of the improvement in the inversion results obtained by increasing the acquisition aperture and (a), using only the low frequency window (i.e., the difference between columns 2 and 4 in Fig. 9), or (b), using the full frequency window (i.e., the difference between columns 3 and 5 in Fig. 9).

Impedance Results

The left column in Fig. 15 contains the true P- and S-impedances for the Marmousi-2 model. The center and right columns contain the recovered P- and S-impedances for the models in Fig. 9 when the Ss and Rs are on the surface only, and along both the surface and the two edges, respectively, for the full 3.09 to 12.218 Hz bandwidth. Fig. 16 contains the corresponding image correlations and the R^2 coefficients between the original and inverted impedances for both of the S/R configurations.

Increasing the aperture increases the ability to invert the deeper, dipping structures in Fig. 15 (compare at the black arrows), and the I_S images have higher resolution than the I_P images from data for a given frequency bandwidth (compare at the green arrows), because range of the S-wave wavenumbers is higher than that of the P-wave wavenumbers.

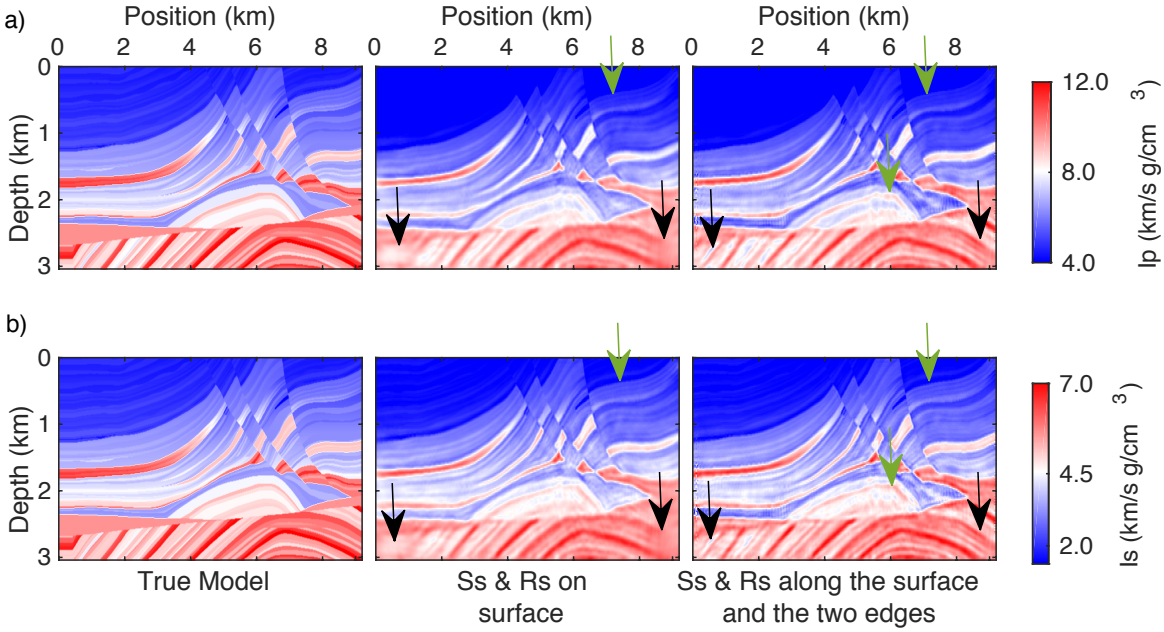

Fig. 15. The true and inverted impedances for (a) I_P and (b) I_S, from the products of the velocity and density results in Fig. 9.

Fig. 16 shows the cross plots between the distributions of data point density in a 61x51 bin, between the original and recovered impedances, for two different configurations. The red lines (in Fig. 16) correspond to the ideal R^2 values (when the true and predicted values are equal). The gray scale gives the data density, the number of data points with the sampling box centered at that location. The P- and S-impedances are fitted better than the velocities and density are separately; the R^2 values for the velocities and densities are all < 0.78 in Fig. 10 and are all > 0.91 for both I_P and I_S in Fig. 16. In the right column of Fig. 16, the wider aperture configuration produces larger R^2 values, because the model is sampled more completely.

DISCUSSION

This study may be viewed as a pilot for future evaluation of acquisition design for optimization of inversion to recover wavenumber information from targets of various wavenumber characteristics. By following procedures similar to those illustrated above, the completeness and uncertainty associated with the FWI images may be quantified. Various combinations of source and receiver space/time (or the equivalent wavenumber/frequency) representations of a target, it's recorded data, and it's spectra, can be simulated prior to field data acquisition to maximize the information recovery, and to quantify the corresponding cost/benefit trade-offs. By modeling and inversion of data simulated for the expected target structures, lithology, and fluid content and spatial distribution, and

perturbing the salient features, quantitative measures can potentially be obtained for the detectability and reliability of the salient aspects of a target. Ozdenvar et al. (1996) illustrate the use of survey simulation for acquisition design by modeling in time and space but did not consider the wavenumber representation. The present study also differs from Vermeer (2012) in that we focus on the relations between the wavenumber characteristic of a target and its reconstruction by FWI, rather than the response functions of the recording arrays only.

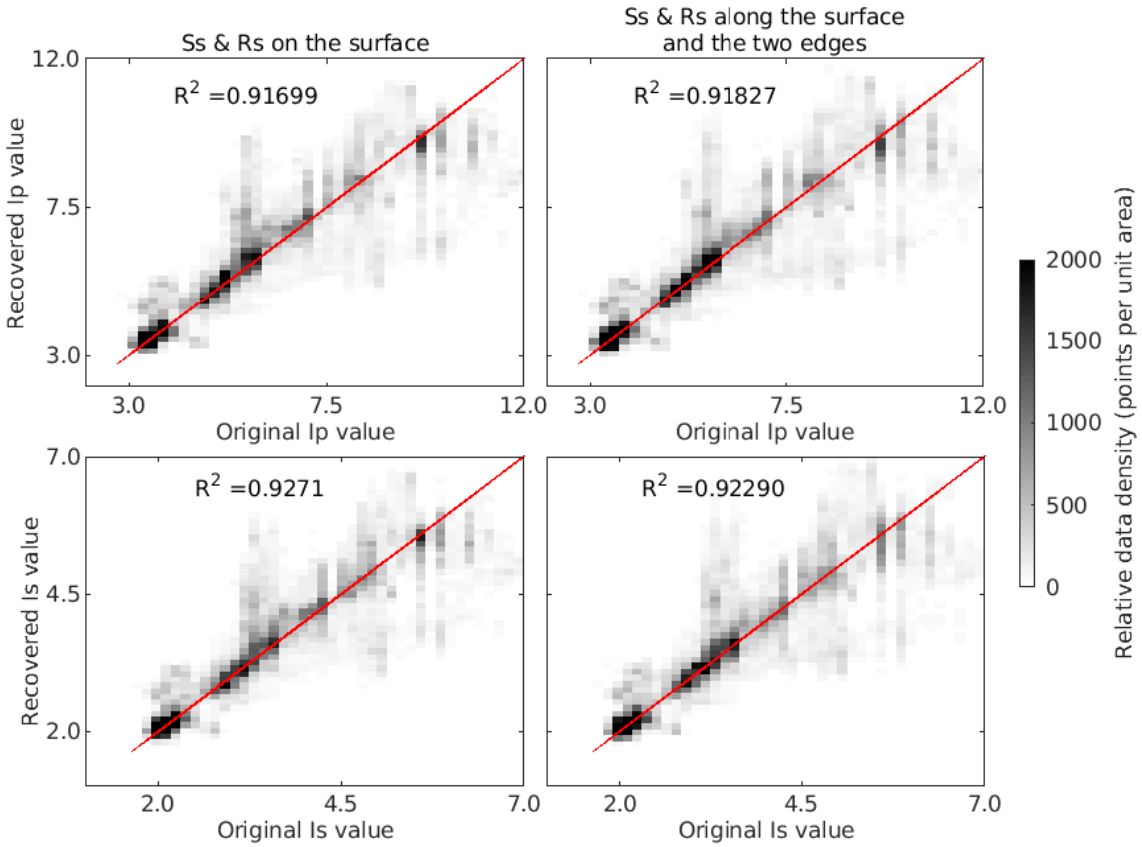

Fig. 16. Cross-plots between original and recovered I_P and I_S wavefield amplitudes for (left) Ss and Rs only on the surface, and (right) for the Ss and Rs on the surface and the two edges. In each panel, the red line is the theoretical location of perfectly recovered impedances. See the description of Fig. 10 in the text for the plot format and the distribution of information. Impedance units are (km/s)(g/cm^3).

The results above use the same source and receiver geometry and source spectra for data simulation and inversion, and so are the best that are achievable for the specific models and data acquisition used. Thus, for example, extending the source frequency band in the inversion, beyond that used to generate the test data in the modeling, would not produce better inversions because the input data would not contain information at those frequencies. In fact, this would result in overfitting of noise at those frequencies.

In the examples above, for the purpose of evaluation of the completeness of the recovered images, it is assumed that the correct solutions are known, so quantitative model misfits can be calculated. In the context of inversion of field data, the correct solution is not known; thus, the residual differences between the observed and calculated data are minimized, and data correlations would replace the model correlations. The best recovered model is then assumed to be the one that minimizes the data misfits. The uncertainty in that model corresponds to the residual data misfit; the model may be nonunique.

One aspect not considered here is the effect of noise in the data, but that has been extensively treated elsewhere. The key observations are that the FWI fits the predictable (coherent) components of the data, but not the (incoherent) noise. Thus, the recovered model is relatively unchanged by the presence of noise, but the residual misfit is determined by the noise level.

It is conceptually straightforward to extend the procedure to 3D models and data. This would require 3D inversion, 3D Fourier transforms and calculation of correlation coefficients from the 3D data and spectral volumes.

CONCLUSIONS

The wavenumber (**k**) bandwidth of an inverted model will always be smaller than that of the correct model because the frequency (ω) of the source wavelet is bandlimited, and any real recording aperture (parameterized by the slowness, **p**) is finite. (The relation between them is $\mathbf{k} = \omega\mathbf{p}$.) To recover a complete model wavenumber spectrum by FWI requires that the illuminating source wavefields contain combinations of wavefront slowness and source frequencies that correspond to all the wavenumbers in the model. Examples using elastic data for a model with a circular anomaly, and for the Marmousi-2 model illustrate these relations. Model misfits are quantified by cross-plotting image correlations and calculating their correlation coefficients. In the Marmousi-2 model example, the impact in model fitting is much larger for increasing the acquisition aperture than for increasing the frequency bandwidth, because of the range of dips in the Marmousi structure. The phase information in the data provides stronger constraints than the amplitude; thus, V_P and V_S are better fitted than density, and velocities tend to be overestimated while density tends to be underestimated. Inverted models typically have smaller wavenumber bandwidths than the correct solution; sharp boundaries in the latter would require frequencies higher than those present in the data to detect, and infinitely-fine wavenumber sampling to represent completely. If the frequencies in the wavelet correspond to wavenumbers higher than those in the model, noise may be overfitted.

ACKNOWLEDGEMENTS

The research leading to this paper is supported by the Sponsors of the UT-Dallas Geophysical Consortium. A portion of the computations were done at the Texas Advanced Computing Center. This paper is Contribution No. 1676 from the Department of Geosciences at the University of Texas at Dallas.

REFERENCES

Alkhalifah, T., 2016. Full-model wavenumber inversion: An emphasis on the appropriate wavenumber continuation. Geophysics, 81(3): R89-R98.

Alkhalifah, T. and Wu, Z., 2016. Multiscattering inversion for low-model wavenumbers. Geophysics, 81(6): R417-R428.

Alkhalifah, T., 2018. Full model wavenumber inversion: Identifying sources of information for the elusive middle model wavenumbers. Geophysics, 83(6): R597-R610.

Berkhout, A.J., 1980. Seismic Migration. Elsevier Science Publishers, Amsterdam.

Berkhout, A.J., Ongkiehong, L., Volker, A.W.F. and Blacquière, G., 2001. Comprehensive assessment of seismic acquisition geometries by focal beams – Part I: Theoretical considerations. Geophysics, 66: 911-917.

Beylkin, G., 1985. Imaging of discontinuities in the inverse scattering problem by inversion of a causal generalized Radon transform. J. Mathem. Phys., 26: 99-108.

Biondi, B. and Almomon, A., 2014. Simultaneous inversion of full data bandwidth by tomographic full-waveform inversion. Geophysics, 79(3): WA129-WA140.

Brossier, R., Operto, S. and Virieux, J., 2009. Seismic imaging of complex onshore structures by 2D elastic frequency-domain full-waveform inversion. Geophysics, 74(6): WCC105-WCC118.

Choi, Y., Min, D. and Shin, C., 2008. Two-dimensional waveform inversion of multicomponent data in acoustic-elastic coupled media. Geophys. Prosp., 56: 863-881.

Devaney, A.J., 1984. Geophysical diffraction tomography. IEEE Transact. Geosci. Remote Sens., GE(22): 3-13.

Devaney, A.J. and Beylkin, G., 1984. Diffraction tomography using arbitrary transmitter and receiver surfaces. Ultrason. Imag., 6: 181-193.

Esmersoy, C., Oristaglio, M.L. and Levy, B.C., 1985. Multi-dimensional Born velocity inversion single wideband point source. J. Acoust. Soc. Am., 78: 1052-1057.

Esmersoy, C. and Levy, B.C., 1986. Multidimensional Born inversion with a wide-band plane wave source. IEEE Proc., 74: 466-475.

Fichtner, A., 2010. Full Seismic Waveform Modelling and Inversion. Springer Verlag, Heidelberg.

Forgues, E. and Lambaré, G., 1997. Parameterization study for acoustic and elastic ray + Born inversion. J. Seismic Explor., 6: 253-278.

Gibson, Jr., L.R. and Tzimeas, C., 2002. Quantitative measures of image resolution for seismic survey design. Geophysics, 67: 1844-1852.

Jeong, W., Lee, H. and Min, D., 2012. Full waveform inversion strategy for density in the frequency domain. Geophys. J. Internat., 188: 1221-1242.

Lailly, P., 1983. The seismic inverse problem as a sequence of before stack migration. Expanded Abstr., SIAM Conf. on Inverse Scattering, Theory and Applications, Philadelphia: 277-289.

Liner, C.L., 2012. Elements of seismic dispersion. A somewhat practical guide to frequency dependent phenomena. Expanded Abstr., 82nd Ann. Internat. SEG Mtg., Las Vegas: 63-65.

McMechan, G.A. and Hu., L.Z., 1986. On the effect of recording aperture in migration of vertical seismic profile data. Geophysics, 51: 2007-2010.

Martin, G.S., Wiley, R. and Marfurt, K.J., 2006. Marmousi2: An elastic upgrade for Marmousi. The Leading Edge, 25: 156-166.
Muerdter, D. and Ratcliff, D., 2001a. Understanding subsalt illumination through raytrace modeling. Part 1: Simple 2-D salt models. The Leading Edge, 20: 578-594.
Muerdter, D. and Ratcliff, D., 2001b. Understanding subsalt illumination through raytrace modeling, Part 3: Salt ridges and furrows, and the impact of acquisition orientation. The Leading Edge, 20: 803-816.
Mora, P., 1987. Nonlinear two-dimensional elastic inversion of multi-offset seismic data. Geophysics, 52: 1211-1228.
Mora, P., 1989. Inversion = migration + tomography. Geophysics, 54: 1575-1586.
Ozdenvar, T., McMechan, G.A. and Chaney, P., 1996. Simulation of complete seismic surveys for optimization of experiment design and processing. Geophysics, 61: 496-508.
Pageot, D., Operto, S., Vallee, M., Brossier, R. and Virieux, J., 2013. A parametric analysis of two-dimensional elastic full waveform inversion of teleseismic data for lithospheric imaging. Geophys. J. Internat., 193: 1479-1505.
Pratt, R.G., Song, Z.-M., Williamson, P. and Warner, M., 1996. Two-dimensional velocity models from wide angle seismic data by wave-field inversion. Geophys. J. Internat., 124: 323-340.
Schuster, G.T. and Hu, J., 2000. Green's function for migration: Continuous recording geometry. Geophysics, 65: 167-175.
Schuster, G.T., Yu, J. and Sheng, J., 2004. Interferometric/daylight seismic imaging. Geophys. J. Internat., 157: 838-852.
Sears, J.T., Barton, P.J. and Singh, S.C., 2010. Elastic full waveform inversion of multicomponent ocean-bottom cable seismic data: Application to Alba Field, U.K. North Sea. Geophysics, 75(6): R109-R119.
Slaney, M. and Kak, A.C., 1983. Diffraction tomography. Proc., SPIE Conf. Inverse Optics, 0413: 2-19.
Shin, C., 1995. Sponge boundary condition for frequency-domain modeling. Geophysics, 60: 1870-1874.
Tarantola, A., 1984. Inversion of seismic reflection data in the acoustic approximation. Geophysics, 49: 1259-1266.
Vermeer, G.J.O., 2012. 3D Seismic Survey Design, 2nd Ed. SEG, Tulsa, OK.
Virieux, J. and Operto, S., 2009. An overview of full-waveform inversion in exploration geophysics. Geophysics, 74(6): WCC127-WCC152.
Volker, A.W.F., Blacquière, G., Berkhout, A.J. and Ongkiehong, L., 2001. Comprehensive assessment of seismic acquisition geometries by focal beams-Part II. Practical aspects and examples. Geophysics, 66: 918-931.
Warner, M., Ratcliffe, A., Nangoo, T., Morgan, J., Umpleby, A., Shah, N., Vinje, V. and Stekl, I., 2013. Anisotropic 3D full-waveform inversion. Geophysics, 78(2): R59-R80.
Wu, R.S. and Toksöz, M.N., 1987. Diffraction tomography and multi-source holography, applied to seismic imaging. Geophysics, 52: 11-25.
Xu, K. and McMechan, G.A., 2014. 2D frequency-domain elastic full-waveform inversion using time-domain modeling and a multistep-length gradient approach. Geophysics, 79(2): R41-R53.
Xu, W., Wang, T. and Cheng, J., 2019. Elastic model low- to intermediate-wavenumber inversion using reflection traveltime and waveform of multicomponent seismic data. Geophysics, 84(1): R109-R123.
Yu, J. and Schuster, G.T., 2003. 3-D prestack migration deconvolution. Expanded Abstr., 73rd Ann. Internat. SEG Mtg., Dallas: 1651-1654.
Yu, J. and Schuster, G.T., 2006. Cross-correlogram migration of inverse vertical seismic profile data. Geophysics, 71(1): S1-S11.